



Synthesis and Characterization of Cu-Incorporated Zinc Tin Zorcinat Thin Film as a Promising Candidate as Absorber Layer in DSSC

Marwa M. Toraya¹, Doaa M. Atia¹, Amany M. El Nahrawy², Ninet M. Ahmed¹, Saleh Hussin³

^aPhotovoltaic Cells Department, Electronics Research Institute (ERI), Cairo, Egypt

^bSolid-State Physics Department, Physics Research Division, National Research Centre, 33 El-Bohouth St., Dokki, 12622, Egypt

^cElectronics and Communications Engineering Department, Faculty of Engineering, Zagazig University, Egypt



CrossMark

Abstract

This study presents the elaboration and characterization of un-doped and Copper co-doped Zinc-Tin-Zirconate (3, 6, 9 mol.%). $Cu_x-ZTZr(2-x)$ nanostructured thin films prepared using sol-gel Copper co-doped Zinc Tin method on a glass substrate and annealed at 500°C for 1hr. The synthesized film samples are characterized by X-ray (XRD), scanning electron microscopy and energy dispersive X-ray (HR-SEM/EDX), Fourier transform infrared spectroscopy (FTIR), and UV-VIS-NIR double beam spectrophotometer. The experimental results demonstrated that all the prepared films exhibited a polycrystalline nanoparticle structure, and the crystallites size was found to be ranged from 17 and 32 nm. SEM micrographs showed scattered nanoparticles with irregular distribution over the substrates, and the particles size is in the range of 21–29 nm. The highly transparent (>85% for doped sample) nanostructures films show a band gap increment from 4 to 4.19 eV with rising Copper content in zinc Tin Zirconate. The effect of Cu focus in ZTZr will differ in the optical properties of the semiconductor, which means that these films have many advantages in solar cell application.

Keywords: Counter electrode, Spin coating, Sol-gel, Optical properties, Dye-sensitized solar cell (DSSC).

1. INTRODUCTION

During the past decade, oxide nanomaterials have acquired much attention owing to their wide potential technological applications in many fields such as gas sensors, solar energy conversions, and as heterogeneous catalysts. One of the most important methods to modify the characteristics of materials that used in photovoltaic fabrication by introducing dopants in the parent system. Among the wide range of semiconducting nanomaterials, zinc oxide (ZnO) is a semiconductor with a wurtzite crystal structure. Zinc oxide with high energy bandgap of 3.35 eV and a large exciton binding energy of 60 meV has been applied in a wide range of applications from sensors to ultra-violet laser diodes and nanotechnology-based devices [1]. A high surface area of porous zinc oxide has also been applied for gas sensor materials [2], biosensors [3], photocatalysts [4], and photoelectrode of dye-sensitized solar cells [5]. Recently, low-cost and high-efficiency counter electrodes (CE) for DSSC were given great attention for development by researchers [6]. In DSSC, CE performs essential functions, which gather electrons from an external circuit and catalyzes the reduction of triiodide ions.

Owing to excellent catalytic activity and ability to produce high power conversion efficiency, Platinum (Pt) has preferred as CE material. However, Pt is scarce and is very expensive which makes it impractical. Furthermore, electrolytes can easily corrode Pt, which reduces the long-term stability of DSSC [7-9]. To substitute Pt, it is necessary to look for economical and stable alternative materials with superior efficiency. A diversity of alternative low-cost materials, for example, organic polymers, carbon materials, and inorganic compounds were discussed in [10-12]. Among the other high-efficiency inorganic transition metal sulfides catalysts that has been verified to be an effective CE materials, e.g. MoS_2 [7], CoS [11, 12], NiS [13- 15], $NiCo_2S_4$ [15, 16], $CuInS_2$ [17, 18], Cu_2ZnSnS_4 (CZTS), Cu_2FeSnS_4 [19], and Cu_2MnSnS_4 [20]. Recently, a lot of research has shed light on the potency of kesterite-structure Cu_2ZnSnS_4 (CZTS) proved to be an effective CE material. In [21], the photovoltaic and electrochemical properties of copper oxide (CuO) and graphene nanostructured copper oxide as CE coated on FTO were investigated. In [22] investigated two different phases of SnO_2 as a CE. The authors of [23]

*Corresponding author e-mail: amany_physics_1980@yahoo.com; (Amany M. El Nahrawy)

EJCHEM use only: Receive Date: 22 July 2021, Revise Date: 14 September 2021, Accept Date: 19 September 2021

DOI: [10.21608/ejchem.2021.87118.4214](https://doi.org/10.21608/ejchem.2021.87118.4214)

©2022 National Information and Documentation Center (NIDOC)

studied nano-fibers of $\text{Cu}_2\text{ZnSnS}_4$ was common as a CE by using polyvinyl pyrrolidone and cellulose acetate as solvents. As a low-cost material, CuSbS_2 and CuInS_2 nano-crystals were also investigated as promising candidates for CEs in DSSC [24, 25]. DSCs based on ZnO-nanostructured have investigated structures to recent date and are the generality efficient ones. Fundamentally ZnO with its higher electron mobility ($115\text{--}155\text{ cm}^2\text{ V}^{-1}\text{ s}^{-1}$), bandgap energy (3.2 eV), and their band locations are similar to those for TiO_2 [26, 27]. Zirconium is outstanding material owing to its high hardness, high temperature stability, low thermal conductivity, and high corrosion resistance [28, 29]. Zirconium thin films have various applications like diffusion barriers, highly transparent films, thermal barrier coating, optical coatings, wear-resistant coatings, and metal cutting applications [30, 31]. Decreasing the particles size and combination of electrons in adherence solar cell system may be one of the promising approaches to enhance their performance for the DSSC. Techniques of deposition used to form thin-film methods span a wide range, which involves sol-gel techniques, sputtering, electro-deposition, screen-printing, spray pyrolysis, and solvothermal method [32-34]. Sol-gel possesses many advantages such as better homogeneity, less energy consumption, no need for special or expensive equipment, very simple, low cost, versatile, and extended composition ranges [35-37]. Thereby, this method is used for the preparation of Copper-Zinc-Tin-Zirconate thin films as CE for DSSCs. In this work, the promising un-doped and copper-doped Zinc-Tin-Zirconate nano-structures thin films were prepared using the facile sol-gel mechanism. The sol-gel-derived spin-films calcined in air at $500\text{ }^\circ\text{C}$ for 1hr. The impact of three different Copper concentrations on the structure, chemical composition, and optical characteristics of synthesized films has been

investigated via XRD, SEM-EDX, FTIR, and UV-VIS spectrophotometry.

2. EXPERIMENTAL WORK

2.1. Synthesize of Nano-Crystalline Zinc Tin Zirconate: Thin Film

Synthesize of nano-crystalline Zinc-Tin-Zirconate thin-film initially, glass substrates were cleaned in ultrasonic with distilled water, acetone for 1 min and dried at $50\text{ }^\circ\text{C}$ on a hot plate for deposition Zinc-Tin-Zirconate (ZTZr) and Zinc Tin Zirconate: Copper (ZTZr: Cu) thin films. Zirconia nitrate $\text{ZrO}(\text{NO}_3)_2 \cdot x\text{H}_2\text{O}$ 99.5%, Zinc-acetate-dehydrate $(\text{CH}_3\text{CO}_2)_2\text{Zn}$, Tin nitrate and Copper nitrate $\text{Cu}(\text{NO}_3)_2 \cdot 2.5\text{H}_2\text{O}$, distilled H_2O and Citric acid as a solution used as starting materials for the preparation of Zinc-Tin-Zirconate and Zinc Tin Zirconate: Copper thin films. All chemicals were analytically pure and prepared without additional purification. Firstly, mix distilled H_2O with citric acid and putting them in the magnetic stirring for 1 hr then adding the mixture to Zinc, Tin, and Zirconate individually to prepare a Zinc-Tin-Zirconate solution. After that add three different concentrations of Copper (3, 6, and 9 at%) to this mixture individually to prepare Zinc Tin Zirconate: Copper solutions. Then, for gelling leave the prepared mixture rest for 10 hr at room temperature (aging step). Facile sol-gel spin-coating mechanisms were applied to deposit the Zinc-Tin-Zirconate and Zinc Tin Zirconate: Copper precursor on an area of $2 \times 2\text{ cm}^2$ glass substrates at 1500 rpm for 30 s. After each layer deposition, all films were preheated at $70\text{ }^\circ\text{C}$ for 5 min in air to evaporate the residual solvents. This step is for gelation and evaporation of the residual solvents, and this process was repeated five times. Finally, all the prepared thin films are annealed at $500\text{ }^\circ\text{C}$ for 1hr in air to obtain dense films shown in Fig 1.

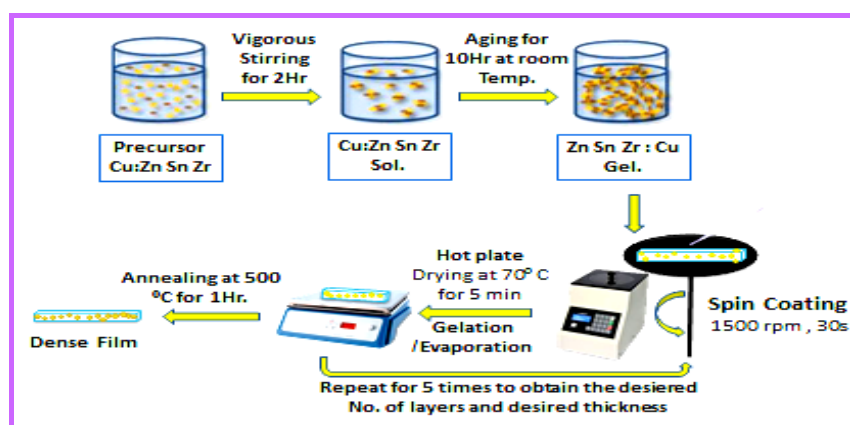


Fig. 1 Block diagram of ZTZr: Cu thin film Cathode fabrication steps

2.2. Characterization

The structure investigation for un-doped and co-doped Zinc-Tin-Zirconate films was performed using a Bruker-D8 advance diffract meter using $\text{CuK}\alpha$ - radiation; $\lambda = 1.540 \text{ \AA}$, operative at 40 mA and 40 kV. Scans were executed with a detector step (0.02°) over an angular range of 10 to 70° . Scherrer's equation for calculation of crystallite size (D) of pure Zinc-Tin-Zirconate and Zinc Tin Zirconate: Copper thin films [26, 38]:

$$D = \frac{(0.9 \lambda)}{(\beta \cos \theta)} \quad (1)$$

Where D is the average grain size along the direction vertical to the certain crystal plane referring to grain size, λ is the X-ray wavelength = 1.54056 \AA , β is the peak width in radians, measured at half the maximum intensity, and θ is the Bragg diffraction angle.

The morphology was observed by scanning electron microscopy (SEM), Hitachi S4800, Japan. The compositional study was measured by EDXRF (Shimadzu EDX-7000). The Fourier Transform Infrared (FTIR)-spectra of samples were recorded with a Bruker-Vector 22 Spectrophotometer fortified with a Specac Golden- GateTM ATR device and working in a spectral range of $4000\text{--}400 \text{ cm}^{-1}$. The transmittance and reflectance measurements were performed by UV-VIS-NIR double beam spectrophotometer (UV-3100, Shimadzu, Japan) providing a wavelength range from 300 to 3000 nm.

3. RESULTS AND DISCUSSIONS

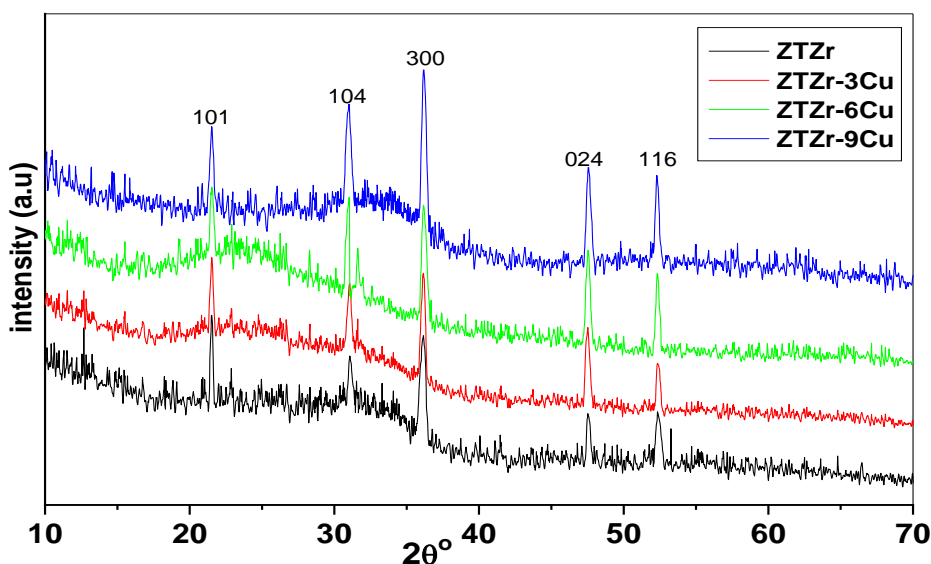


Fig 2 XRD patterns of un-doped ZTZr and $\text{Cu}_x\text{-ZTZr}_{(2-x)}$.

3.1. X-Ray Diffraction

Figure 2 shows the crystalline phase of the post-growth of pure Zinc-Tin-Zirconate and doped with (3-9 mol%) Copper prepared by sol-gel processes and thermally treated at temperature 500°C . The resulted XRD peaks are corresponding to the two crystalline phases of Tin Zirconium and Zinc Tin oxides cards 65-0517 and 52-1381, respectively. It can be observed that Zinc-Tin-Zirconate and doped with Copper show the main XRD peak at $\sim 36.4^\circ$, with a good film crystallinity. The crystallite sizes were extracted from the width of (211) diffraction peak at 36.4° . The XRD analysis showed that the calculated crystallite size of the material is obtained using the Scherrer equation, which values are between 17 nm and 32 nm for a 3% Copper concentration. At 3% copper concentration, it can be detected that the crystallite size value was the maximum and further declined at higher Copper concentrations (6% & 9%). The average crystallite size is increased from 17 to 32 nm by adding 3% Copper whereas the 9% Copper incorporated sample has 28.19 nm. The reduction in crystallite size is mainly due to distortion in Zinc-Tin-Zirconate by the foreign impurity, i.e. Cu^{+2} which decrements the nucleation and subsequent the good film crystallinity. This result appears that the Zinc-Tin-Zirconate and Zinc Tin Zirconate: Copper nuclei are further tending to higher growth at the lower Copper concentration.

3.2. Films Morphology

The morphology of Zinc-Tin-Zirconate and Zinc-Tin-Zirconate-Copper thin film surfaces is carried out by SEM micrographs. Figure 3 (a and b) shows the surface morphology of pure and 6% Copper co-doped Zinc-Tin-Zirconate films deposited on a glass substrate. The SEM images exhibit the polycrystalline nature of the layers and scattered nanoparticles with an irregular (random) distribution over the substrates. Figure 3(a) shows the morphology of pure Zinc-Tin-Zirconate film representative of a mixture of square-like and indistinct (irregular) shaped nanoparticles in addition to a few clusters of nanoparticles and a few large nanoparticles observed on the film surface. The grain size was in the range of 27.78–37.5 nm. @ 6% Copper concentration as shown in Fig. 3(b), the grain size is decreased where film surface morphology became less dense, and randomly oriented square-like nanoparticles with 21.6 nm - 28.3 nm as average size were observed. These results matched with the previously obtained results of the XRD. EDX patterns of the un-doped and Copper –doped Zinc-Tin-Zirconate films are shown in Fig 3(c, d). The EDX spectra confirm that all constitute elements Zinc, Tin, and Zirconate appear in the spectrum at specific values of energy in addition to the presence of Copper in the doped films. The actual atomic percentages of the respective elements are explained in the inserted tables. The values show the incorporated Copper resulted in the reduction of Zinc and Zirconate atomic percentage.

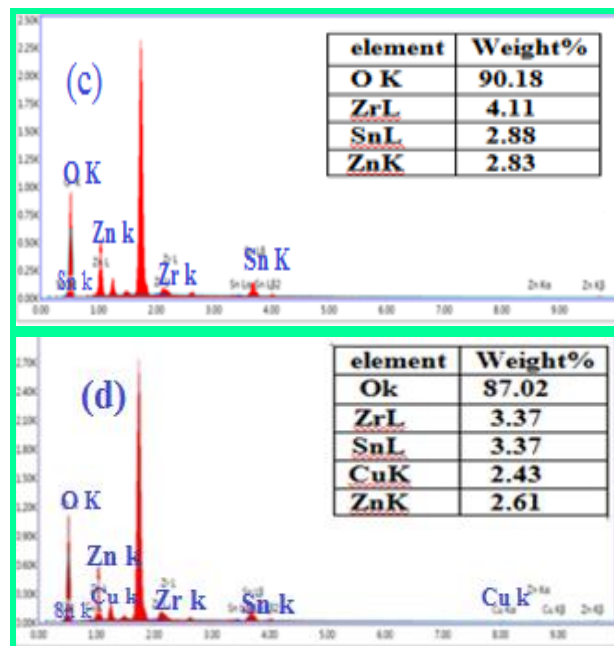
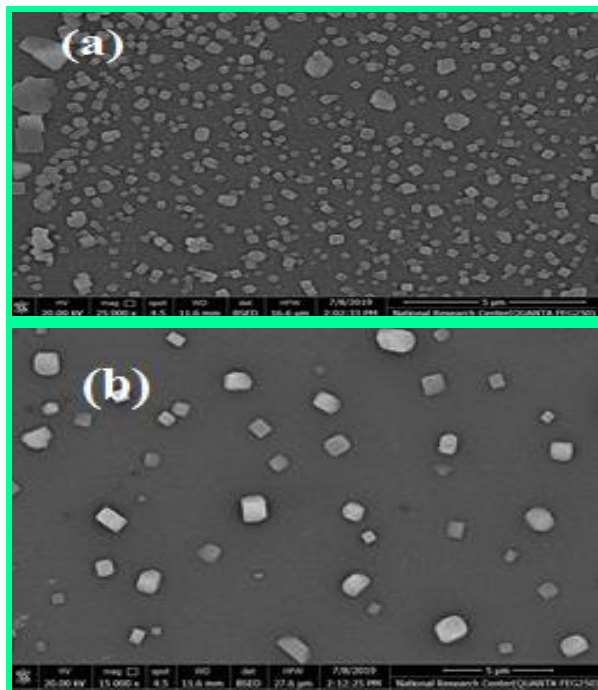


Fig 3. The surface morphology of (a) un-doped ZTZr film (b) 6% mol ZTZr: Cu (c) EDX pattern of the un-doped (d) EDX pattern of the Cu-doped ZTZr films.

3.3. Fourier Transform Infrared (FTIR)

FTIR spectrophotometer is probably the main tool for identifying chemical bonds. FTIR spectra of (a) un-doped Zinc-Tin-Zirconate and Copper co-doped Zinc-Tin-Zirconate thin films at (b) 3%, (c) 6%, and (d) 9% Copper concentrations in the wavenumber range of 2000 to 400 cm^{-1} presented in Fig. 4. The un-doped Zinc-Tin-Zirconate thin film exhibits six transmission peaks around 441 cm^{-1} , 527 cm^{-1} , 767 cm^{-1} , 921 cm^{-1} , 1085 cm^{-1} and 1595 cm^{-1} . The weak peak at $\approx 1595 \text{ cm}^{-1}$ is assigned to H–O–H stretching vibration [34, 35]. The shoulder at $\approx 1085 \text{ cm}^{-1}$ and the band at 921 cm^{-1} is related to the (Zinc/Zirconium/Tin)–oxygen stretching vibrations within the range of 1100 - 400 cm^{-1} [41, 42]. The main characteristics peaks for Zinc-Tin-Zirconate and Zinc Tin Zirconate: copper films are 921 cm^{-1} , 767 cm^{-1} , 527 cm^{-1} , and 474 cm^{-1} as the metal oxides vibrations. The peak around $\approx 767 \text{ cm}^{-1}$ can attribute to asymmetric vibration of the Zr–O–Zr bond [43]. The vibration at 527 cm^{-1} is related to the terminal oxygen vibration of Sn–OH in the Zinc-Tin-Zirconate matrix. The Zn–O, Zr–O, and Sn–O bonds were assigned to stretching frequency at 474 cm^{-1} shifted to a lower wavenumber at 441 cm^{-1} with increasing the Copper concentration [44, 45]. This could attribute to the change in the microstructural features by adding Cu into Zn–O lattice.

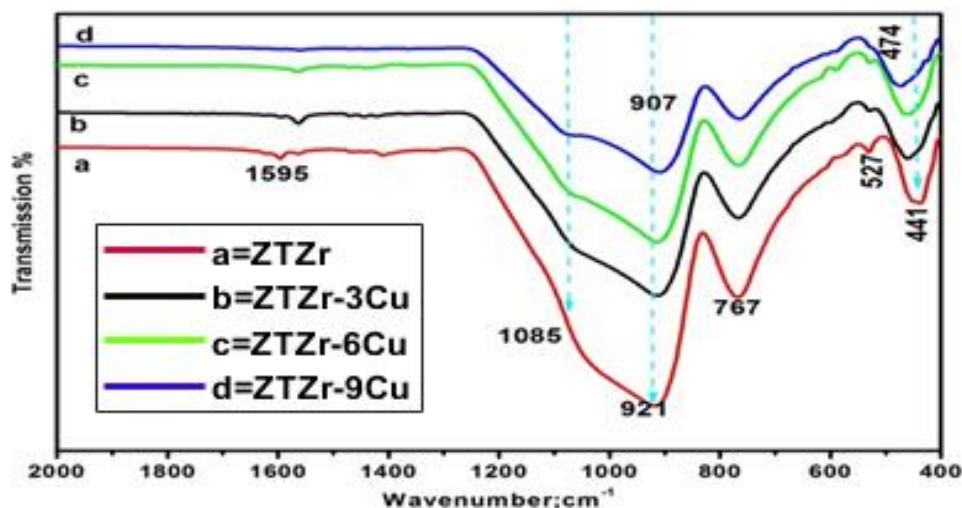


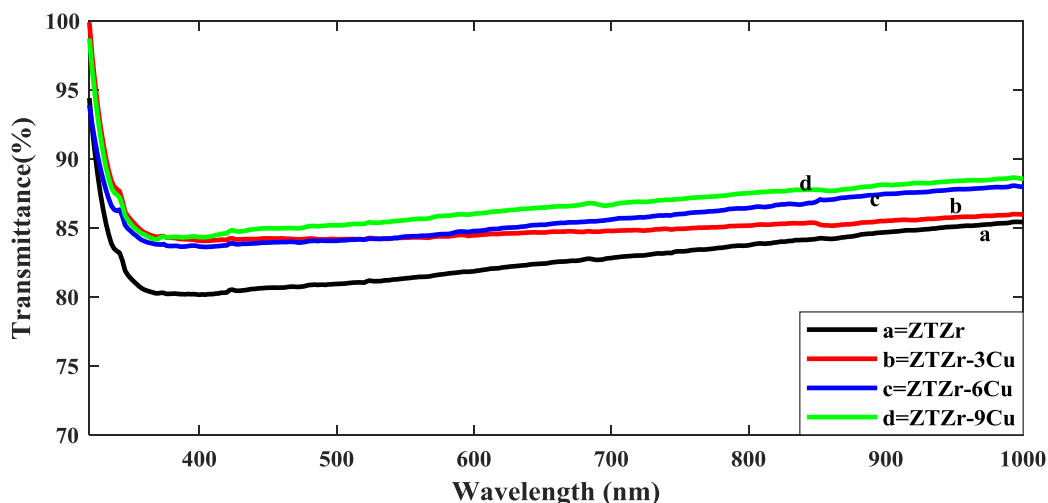
Fig 4 FTIR patterns of un-doped ZTZr and ZTZr: Cu thin films

3.4. Optical Properties

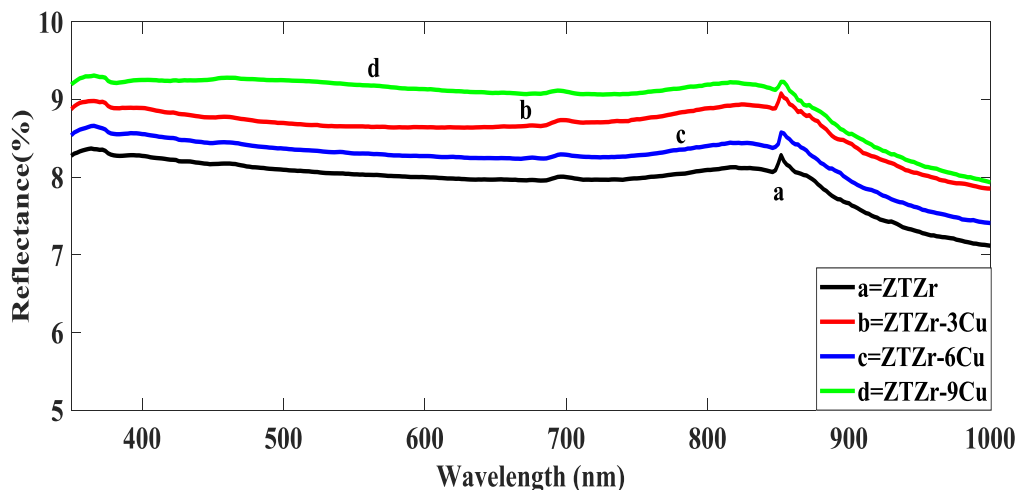
3.4.1. Transmission and Reflection

The transmittance spectra of un-doped Zinc-Tin-Zirconate and Cu co-doped with 3%, 6%, and 9% for five layers measured at 300–2000 nm wavelength are shown in Fig 5. All the films show high transmittance in the visible and infrared regions of the electromagnetic spectrum. These spectra show that adding Copper to the mixture of Zinc-Tin-Zirconate increases the transmittance for all the deposited samples. Despite the maximum value of the transmittance lying in the NIR spectral region exceeds 85%, the un-doped films show a transmittance of 86.33% (550 nm) and the doping process increases transmittance value up to 90.54%

(550 nm) for 9% Copper doping. The increased optical transmittance is due to the crystallinity of the film. The reflectance spectra of un-doped and Cu co-doped Zinc-Tin-Zirconate thin films are inserted in Fig 5. It is evident that there is a sharp increase in the reflectivity of undoped and Copper-doped Zinc-Tin-Zirconate films around transition edge followed by an insignificant reduction with the wavelength in the visible and NIR then it reduces at higher wavelengths. Also, the reflectance of the Zinc-Tin-Zirconate thin films irregularly increases with increasing Copper concentration and reflectance of the film with the 9% Copper incorporation is the highest value, while the reflectance of the un-doped Zinc-Tin-Zirconate thin film is the lowest value.



(a)



(b) Fig 5. The un-doped ZTZr and Cu co-doped ZTZr (a) Transmittance spectra (b) reflection variation with the wavelength.

3.4.2. Absorption Coefficient

The absorption coefficients (α) of undoped and Copper doped Zinc-Tin-Zirconate films can be calculated from both the transmittance (T) and film thickness (t) using the following equation [47]:

$$\alpha = \frac{\ln(1/T)}{t} \quad (2)$$

The variation of the absorption coefficients as a function of wavelength of un-doped and Copper co-

doped Zinc-Tin-Zirconate films is shown in Fig 6. It is found that the absorbance decreases with an increase in wavelength and an increase in Copper doping concentration. The sharp increments in absorbance coefficients at the wavelength $\lambda \leq 500$ nm are owing to the onset of interband transitions at the fundamental edge. This decrease in α might be due to the increase in surface smoothness which might be due to the improved crystallinity of the Cu incorporated thin film.

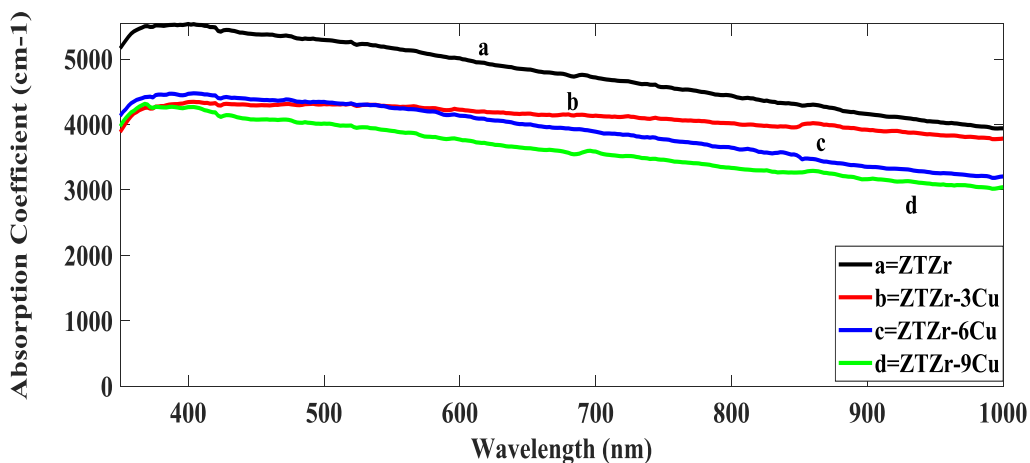


Fig 6. The absorption coefficient variation with the wavelength of the un-doped and Cu co-doped ZTZr films.

3.4.3. Band Gap

The values of the band gap were calculated by the essential absorption, which corresponds to electron excitation from the valance band to the conduction band. The absorption coefficient (α) and the incident

photon energy ($h\nu$) are related by using the Tauc relation [49, 50] :

$$(\alpha h\nu)^2 = A(h\nu - E_g) \quad (3)$$

Where A is constant, E_g is the band gap. The band gap values can be calculated by extrapolating the linear part of the figure of $(\alpha h\nu)$ versus $h\nu$ as shown in Fig 7. The optical energy gap values for Zinc-Tin-Zirconate and Zinc Tin Zirconate: Copper thin films were (4.1, 4.15, 4.04 and 4.19) eV for Copper concentration (0, 3, 6 & 9) respectively. It noticed that the bandgap is not affected obviously by the doping concentration. The high estimated values of band gaps may result from the presence of the ZrO_2 phase

which causes the enlargement of the optical band gap since this phase has a large bandgap around 5.5 eV. The variation in the optical band gap of Zinc-Tin-Zirconate after Copper doping could be related to the structural modification of Zinc-Tin-Zirconate films which may be from the replacement of either substitutional or interstitial zinc ions in the Zinc-Tin-Zirconate lattice by Copper ions. In addition, the greatest possible reason behind the energy gap behavior is the effect of particle size.

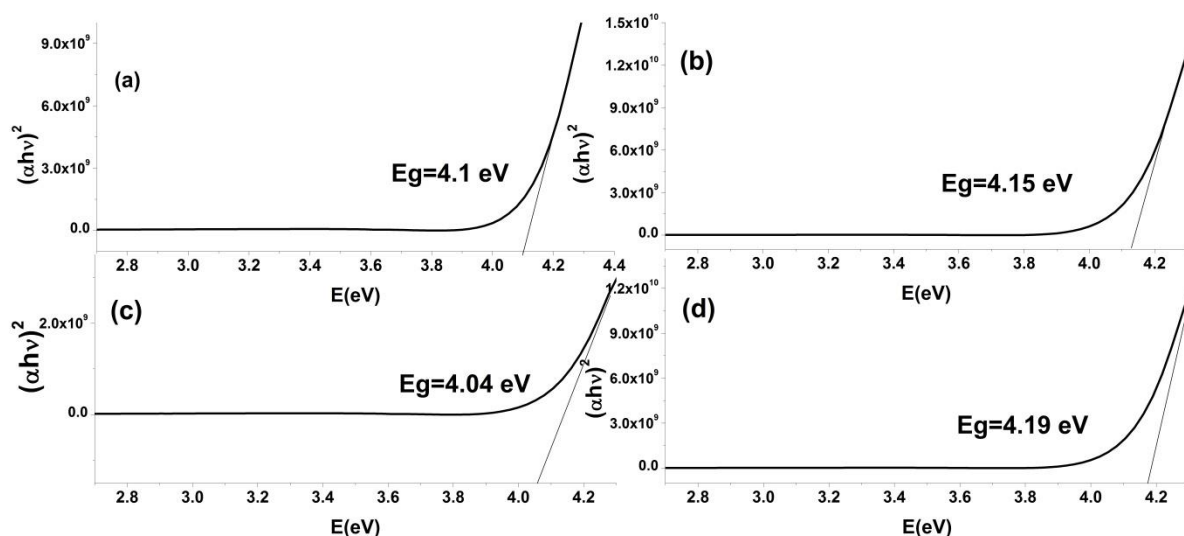


Fig 7 The plots of $(\alpha h\nu)^2$ vs. photon energy (a) the undoped ZTZr thin films (b) 3% Cu-doped ZTZr thin films (c) 6% Cu-doped ZTZr thin films, and (d) 9% Cu-doped ZTZr thin films.

3.4.4. Extinction Coefficients and Refractive Index

The extinction coefficients (k) for undoped and Copper doped Zinc-Tin-Zirconate films were calculated from the following relation [48, 49]:

$$K = \frac{\alpha \lambda}{4\pi} \quad (4)$$

Where α is the absorption coefficient, λ is the incident photon wavelength. Also, the refractive index (n) of the prepared film can be calculated in terms of reflection (R) and the extinction coefficients (k) according to the Fresnel equation [48, 49]:

$$n = \frac{1+R}{1-R} + \sqrt{\frac{4R}{(1-R)^2} - K^2} \quad (5)$$

The extinction coefficient variation with wavelength was given in Fig 8. This figure exhibits an abrupt

reduction of extinction coefficient for all samples around the band edge and it is approximately constant with an increase in wavelength. In addition, it is observed that, unsystematic change in the Zinc-Tin-Zirconate thin films extinction coefficient with a regular increase in Copper doping concentration. The extension coefficient of 3% Copper doped Zinc-Tin-Zirconate thin film is the highest value, while that of 6% Copper doped Zinc-Tin-Zirconate thin film has the lowest value of all the films. Also, the refractive index dependence on the incident photon wavelength is described in Fig 9. It observed that the refractive index slightly reduces with wavelength and considerable increases with Copper concentration. The estimated values of refractive index at a wavelength around 500 nm are 1.81 and 1.88 for undoped and 9% Copper concentration, respectively. The refractive index increases with increasing Cu dopant. This effect of Cu doping on the refractive index of ZTZr films can be attributed to the decrease of both polarizability and film density.

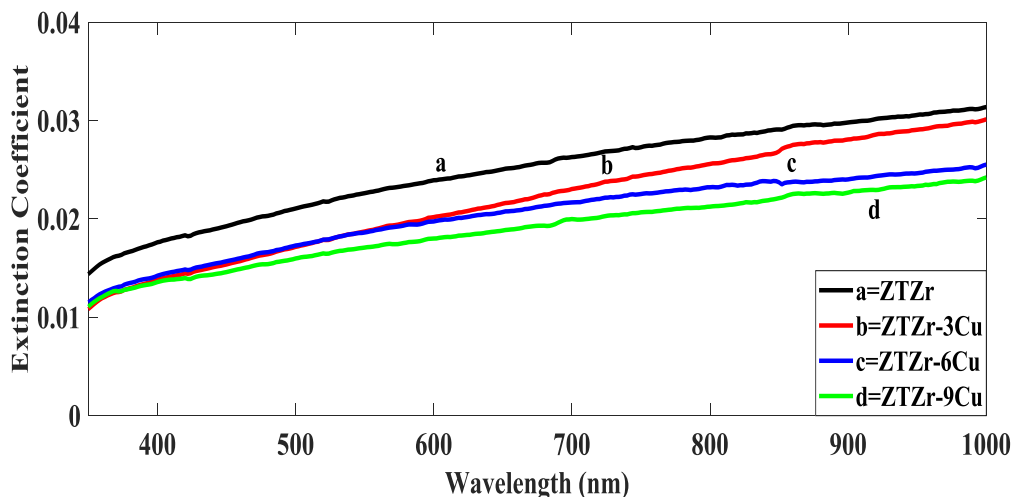


Fig 8. The extinction coefficients variation with the wavelength of un-doped and Cu co-doped ZTZr films.

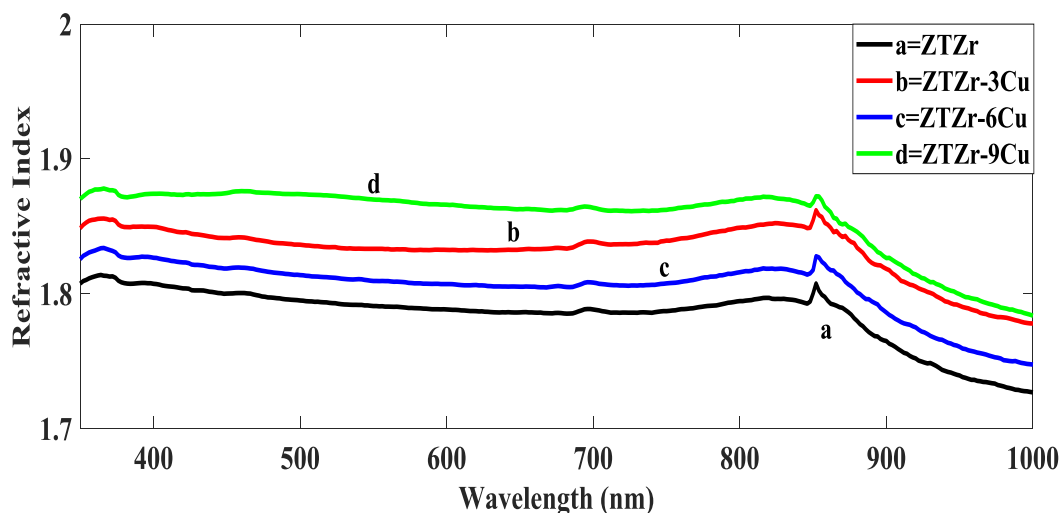


Fig 9. The refractive index variation with wavelength of un-doped and Cu co-doped ZTZr films.

3.4.5. Dielectric Constants

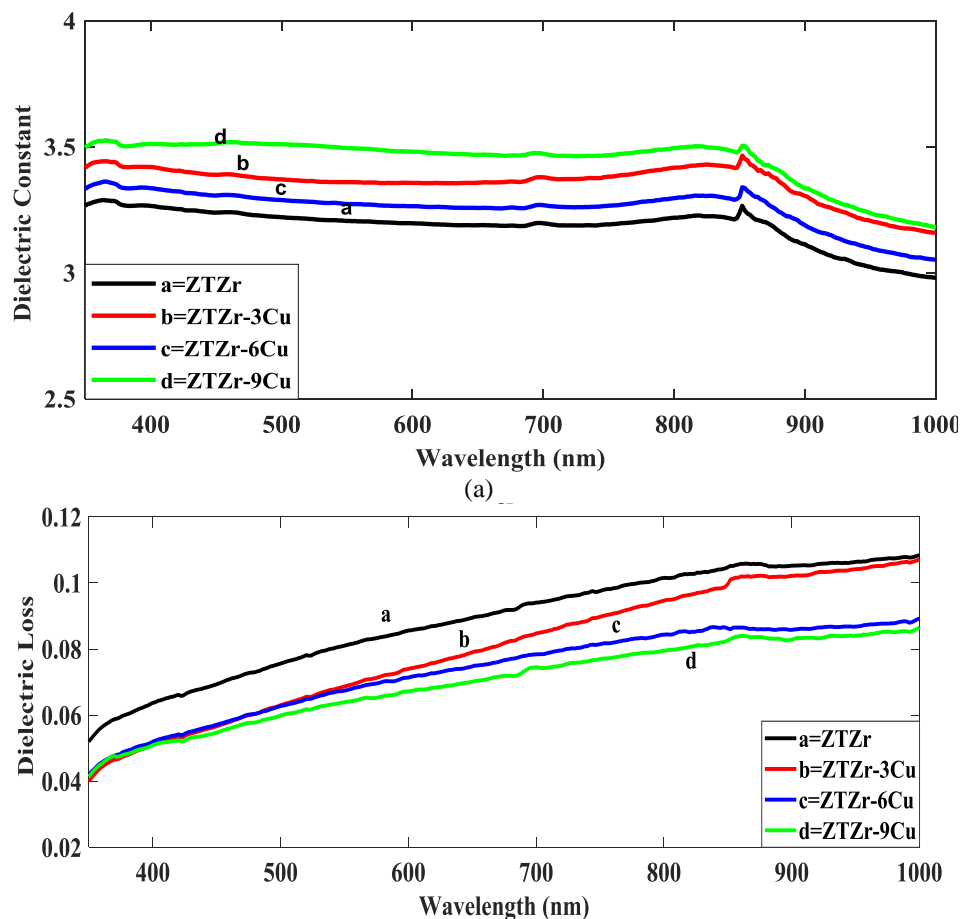
The real part of the dielectric constant (ϵ_r) is to measure how much that material will slow down the light speed and the dielectric constant imaginary part (ϵ_i) is used to express how much energy results from the electric field absorbed by the dielectric material due to dipole motion. The real part (ϵ_r) is associated with the refractive index (n) in the material. The imaginary part of the dielectric constant (ϵ_i) is related to the extinction coefficient (k), or in other words with the absorption of light in the material as described in the following relations [50]:

$$\epsilon = \epsilon_i + \epsilon_r \quad (6)$$

$$\epsilon_i = 2 n K \quad (7)$$

$$\epsilon_r = n^2 - K^2 \quad (8)$$

Figure 10 displays the variation of the real (ϵ_r) and imaginary (ϵ_i) parts of the dielectric constant against photon's energy ($h\nu$). It is indicated that ϵ_r follows the behavior of the refractive index (n) and ϵ_i follows the behavior of the extinction coefficient (k). The real part of the dielectric constant abruptly increases around the band edge then starts to decrease slowly with wavelength and their values increase from 3.22 to 3.51 at the wavelength of 500 nm. While the imaginary part decreases with increasing wavelength and their values are found to decrease from 0.034 to 0.018 at the wavelength of 500 nm.



(b)

Fig 10. The variation of real and imaginary parts of the dielectric constants of un-doped and Cu co-doped ZTZr films.

3.4.6. The Optical Conductivity

The optical response is mainly studied for any material in terms of optical conductivity (σ_{opt}). The optical conductivity is closely related to the energy band structure of the deposited films. The optical conductivities of un-doped and Cu doped ZTZr thin films can be calculated by using the absorption coefficient (α) as in the following equation:

$$\sigma_{opt} = \frac{\alpha n c}{4\pi} \quad (9)$$

Where n is the refractive index and c is the velocity of light. Figure 11 shows the variation of optical conductivity as a function of photon wavelength. The optical conductivity decreases with increasing Cu concentration. This behavior can be attributed to the absorbance decrease with increasing in wavelength and increasing in Cu doping concentration.

3.4.7. Loss Tangent

The dielectric loss tangent ($\tan \delta$) of un-doped and Cu doped ZTZr thin films, which represent how the

electric energy dissipated into thermal energy and can be defined by:

$$\tan \delta = \frac{\epsilon_i}{\epsilon_r} \quad (10)$$

Where δ is the phase angle between the electric field and the polarization of the dielectric, ϵ_r and ϵ_i are the real and imaginary parts of the dielectric constant, respectively. The variation of dielectric loss tangent of un-doped and Cu -doped ZTZr thin films with photon wavelength is shown in Fig. 12. It is seen that the loss tangent decreases with Cu concentration increment while it is almost constant with increasing the photon wavelength and the change in the $\tan \delta$ is dominated by the variation of ϵ_i .

3.4.8. Quality Factor

The Q-factor of un-doped and Cu -doped ZTZr thin films can be calculated from tangent losses using the following equation:

$$[Q = \frac{1}{\tan \delta}] \quad (11)$$

The dependence of quality factor of un-doped and Cu -doped ZTZr thin films on photon wavelength is illustrated in Fig. 13.

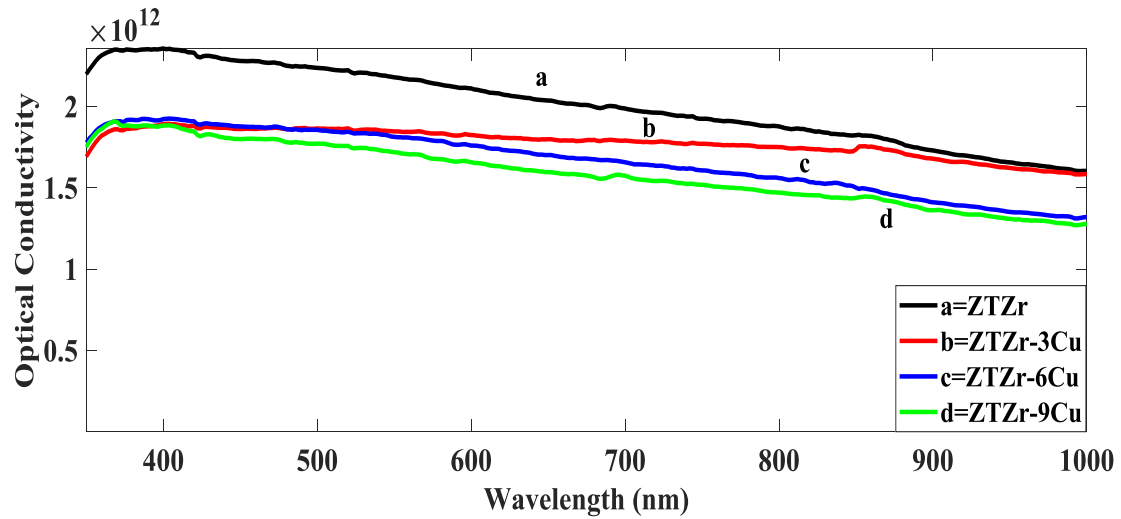


Fig 11. The optical conductivity variation with wavelength of un-doped and Cu co-doped ZTZr films.

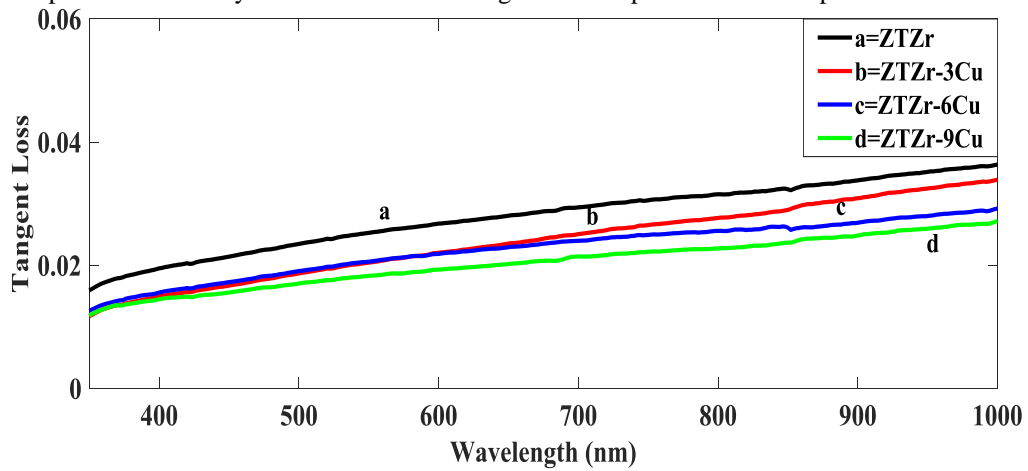


Fig 12. The tangent loss variation with wavelength of un-doped and Cu co-doped ZTZr films.

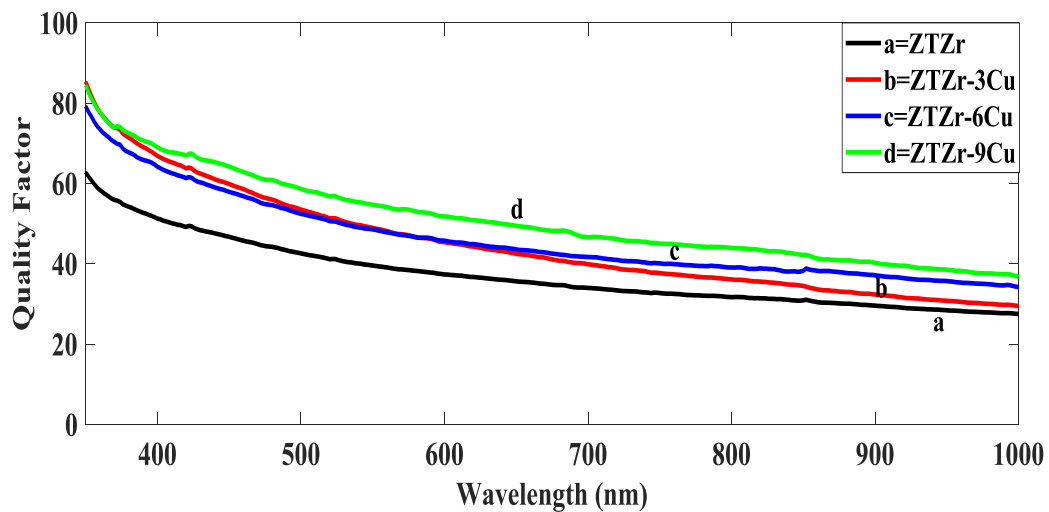


Fig 13. The quality factors variation with wavelength of un-doped and Cu co-doped ZTZr films.

4. CONCLUSION

Un-doped and Copper co-doped Zinc-Tin-Zirconate thin films on a glass substrate were deposited at different Copper concentrations (3%, 6%, 9%) calcined for 1 hr at 500 °C. Adding Copper to the Zinc-Tin-Zirconate matrix has affected structure significantly, surface morphology, optical and physical properties. Kesterite structure of un-doped Zinc-Tin-Zirconate and Copper co-doped Zinc-Tin-Zirconate thin films based sol-gel technique were successfully synthesized. The nanoparticles size decreased at high concentrations of doping. The un-doped and Copper co-doped Zinc-Tin-Zirconate films show a high bandgap within the range of 4.05 - 4.19 eV were obtained. The transparency has improved by adding Copper to the Zinc-Tin-Zirconate matrix; the transmission varied between 85% to 90%. The chemical and physical structure, moreover optical results showed that Zinc Tin Zirconate: Copper thin-film nanoparticles were successfully prepared. The high transparency of prepared samples may be suitable for particular solar cell applications as a transparent window.

References

- [1] Cao, X. Teng, H. Heo, Y. Li, O. Cho, G. Li, W. Cai. Different ZnO nanostructures fabricated by a seed-layer assisted electrochemical route and their photoluminescence and field emission properties. *J. Phys. Chem. C*, 2007, Vol. 111, pp. 2470-2476.
- [2] Huang, J., W. Chao, F. Shieu. Characteristics of zinc oxide crystallites deposited on ITO for dye-sensitized solar cells. *J. Chin. Chem. Soc.*, 2010, Vol. 57, pp. 1200-1203
- [3] Hariharan, C. Photocatalytic degradation of organic contaminants in water by ZnO nanoparticles: Revisited. *Applied Catalysis A: General*, 2006, Vol. 304, pp. 55-61.
- [4] Jagadish, C., S. Pearton, 2006. *Zinc Oxide Bulk, Thin Film and Nanostructures: Processing, Properties and Applications*. Elsevier, Amsterdam.
- [5] Jain, A., P. Sagar, R. Mehra, 2007. Changes of structural, optical and electrical properties of sol-gel derived ZnO films with their thickness. *Mater. Sci.-Poland*, 2006, Vol. 25, pp. 233-242.
- [6] Zinatloo, S., Salehi, Z., Salavati, M., Green synthesis and characterization of Dy₂Ce₂O₇ nanostructures using Ananas comosus with high visible-light photocatalytic activity of organic contaminants, *Journal of Alloys and Compounds*, Vol. 763, 2018, PP. 314-321.
- [7] Martinson, F., Hamann, W., Pellin, J., Hupp, T., New architectures for dye sensitized solar cells, *Chem.-Eur. J*, Vol. 14, 2008 , PP.4458-4467.
- [8] Xu, C., Wu, J., Desai, V., Gao, D., Am, J., Multilayer assembly of nanowire arrays for dye-sensitized solar cells. *J. Am. Chem. Soc.*, Vol. 133, 2011, PP. 8122-8125.
- [9] Xu, C., Shin, H., Cao, L., Wu, J., Gao, D., Ordered TiO₂ nanotube arrays on transparent conductive oxide for dye-sensitized solar cells, *Chem. Mater*, Vol. 22, 2010, PP.143-148.
- [10] Gong, J., Sumathy, K., Qiao, Q., Zhou, Z., Review on dye-sensitized solar cells (DSSCs): Advanced techniques and research trends, *Renewable and Sustainable Energy Reviews*, Vol. 68, Part 1, 2017, PP. 234-246.
- [11] Nazeeruddin, M., Baranoff, E., Gratzel, M., Dye-sensitized solar cells: A brief overview. *Solar Energy*, Vol. 85, 2011, PP. 1172-1178.
- [12] Margulis, Y., Lim, B., Hardin, E., Unger, L., Jun-Ho, Y., Feckl, M., Fattakhova-Rohlfing, D., Bein, T., Gratzel, M., Sellinger, A., McGehee, D., Highly soluble energy relay dyes for dye-sensitized solar cells. *Phys. Chem.*, Vol. 15, 2013, PP. 11306-11312.
- [13] Vijaya, S., Landi, G., Wu, J., Anandan, S., MoS₂ nanosheets based counter electrodes: An alternative for Pt-free dye-sensitized solar cells, *Electrochimica Acta*, Vol. 294, 2019, pp. 134-141
- [14] Ahmad, S., Yum, J., Butt, H., Nazeeruddin, M., Gratzel, M., Efficient Platinum-Free Counter Electrodes for Dye Sensitized Solar Cell Applications *Chem. Phys. Chem*, Vol. 11, 2010, PP. 14-19.
- [15] Sajeesh, T., Spray Pyrolysed Tin Chalcogenide Thin Films: Optimization of optoelectronic properties of SnS for possible photovoltaic application as an absorber layer, 2012, Ph.D. thesis, Cochin University of Science and Technology.
- [16] Wu, M., Lin, X., Wang, T., Qiu, J., Ma, T., *Energy Environ. Sci*. Low-cost dye-sensitized solar cell based on nine kinds of carbon counter electrodes, Vol. 4, 2011, PP. 8-15.
- [17] Lee, K., Lee, H., Wang, D., Park, N., Lee, J., Park, O., Park, J., Dye-sensitized solar cells with Pt- and TCO-free counter electrodes, *Chem. Commun*. Vol.46, 2010, PP. 5-7.
- [18] Kavan, L., Yum, J., Grätzel, M., Graphene nanoplatelets outperforming platinum as the electrocatalyst in co-bipyridine-mediated dye-sensitized solar cells, *Nano Lett*. Vol. 11, 2011, PP. 1-6.
- [19] X. Chen, Y. Hou, B. Zhang, X. H. Yang, H. Yang, Low-cost SnS_x counter electrodes

- for dye-sensitized solar cells, *Chem. Commun.* Vol. 49, 2013, PP. 93-95.
- [20] Chen, X., Hou, Y., Zhang, B., Yang, X., Yang, H., J. Mater. Chem., Sol-gel synthesis and photoluminescent properties of cerium-ion doped yttrium aluminum garnet powders Vol.12, 2002, PP.25-30.
- [21] Tsai, C.-H., Fei, P.-H., Lin, C.-M., Shiu, S.-L., 2018. CuO and CuO/graphene nanostructured thin films as counter electrodes for Pt-free dye-sensitized solar cells. *Coatings* 8, 21.
- [22] Pan, J., Wang, L., Jimmy, C.Y., Liu, G., Cheng, H.-M., 2014. A nonstoichiometric $\text{SnO}_2 - \delta$ nanocrystal-based counter electrode for remarkably improving the performance of dye-sensitized solar cells. *Chem. Commun.* 50, 7020–7023.
- [23] Mali, S.S., Patil, P.S., Hong, C.K., 2014. Low-cost electrospun highly crystalline kesterite $\text{Cu}_2\text{ZnSnS}_4$ nanofiber counter electrodes for efficient dye-sensitized solar cells. *ACS Appl. Mater. Interfaces* 6, 1688–1696.
- [24] Ramasamy, K., Tien, B., Archana, P., Gupta, A., 2014. Copper antimony sulfide (CuSbS_2) mesocrystals: a potential counter electrode material for dye-sensitized solar cells. *Mater. Lett.* 124, 227–230.
- [25] Yao, R.-Y., Zhou, Z.-J., Hou, Z.-L., Wang, X., Zhou, W.-H., Wu, S.-X., 2013. Surfactant-free CuInS_2 nanocrystals: an alternative counter-electrode material for dye-sensitized solar cells. *ACS Appl. Mater. Interfaces* 5, 3143–3148.
- [26] Yuan, K., Yin, X., Li, G., Wu, J., Wang, Y., Huang, F., Preparation and DSC application of the size-tuned ZnO nanoarrays, *J. Alloy Compd.*, Vol. 489, 2010, PP. 94–99.
- [27] Saber, S., Mollar, M., El Nahrawy, A., Khattab, N., Eid, A., Abo-Aly, M., Mar, B., Annealing study of electrodeposited CuInSe_2 and CuInS_2 thin films, *Opt Quant Electron* 50, Vol. 248, 2018.
- [28] El Nahrawy, A., Elzwawy, A., Alam, M., Hemdan, A., Asiri, A., Karim, M., Abou Hammad, A., Rahman, M., Synthesis, structural analysis, electrochemical and antimicrobial activities of copper magnesium zircono silicate ($\text{Cu}_{20}\text{Mg}_{10}\text{Si}_{40}\text{Zr}_{(30-x)}\text{O}:(x = 0,5,7,10) \text{Ni}^{2+}$) nanocrystals, *Microchemical Journal*, Vol. 163, 2021.
- [29] Sivakumar, S., Praveen, K., Shanmugavelayutham, G., Preparation and thermophysical properties of plasma sprayed lanthanum zirconate, *Materials Chemistry and Physics*, Vol. 204, 2018, PP. 67-71.
- [30] Yugeswaran, S., Yoganand, C., Kobayashi, A., Paraskevopoulos, K., Subramanian, B., Mechanical properties, electrochemical corrosion and in-vitro bioactivity of yttria stabilized zirconia reinforced hydroxyapatite coatings prepared by gas tunnel type plasma spraying. *Journal of the Mechanical Behavior of Biomedical Materials*, 2012 Vol., 9, PP., 22-33.
- [31] Mauer, G., Sebold, D., Va Ben, R., Stover, D., Improving Atmospheric Plasma Spraying of Zirconate Thermal Barrier Coatings Based on Particle Diagnostics. *J Therm Spray Tech*, Vol. 21, 2012, PP. 363–371.
- [32] Dahshan, A., Abou Hammad, A., Aly, K., El Nahrawy, A., Eu_2O_3 role in the optical and photoluminescence properties of $50 \text{SiO}_2 - 7 \text{MgO} - 20 \text{ZnO} - (23 - x) \text{La}_2\text{O}_3 - x \text{Eu}_2\text{O}_3$ nanocrystalline thin films, *Appl. Phys. A*, Vol. 126, 2019, PP. 1-8.
- [33] Hara, K., Horoguchi, T., Kinoshita, T., Sayama, K., Sugihara, H., Arakawa, H., Highly efficient photon-to-electron conversion of mercurochrome-sensitized nanoporous ZnO solar cells, *Chem. Lett.*, 2000, Vol. 64, PP. 316–317.
- [34] Zhao, J., Lu, X., Zheng, Y., Bi, S., Tao, X., Chen, J., Zhou, W., Eu doping for hierarchical ZnO nanocrystalline aggregates based dye-sensitized solar cell, *Electrochemistry Communications*, Vol. 32, 2013, PP. 14–17
- [35] El Nahrawy, A., Hemdan, B., Abou Hammad, A., Abia, A., Bakr, A., Microstructure and Antimicrobial Properties of Bioactive Cobalt Co-Doped Copper Aluminosilicate Nanocrystallines, *Silicon*, Vol.12, 2020, PP.17-27.
- [36] Abou Hammad, A., Elnahrawy, A., Youssef, A., Youssef, A., Sol gel synthesis of hybrid chitosan/calcium aluminosilicate Nanocomposite membranes and its application as support for CO2 sensor, *International Journal of Biological Macromolecules*, Vol.125, 2019, PP. 503–509.
- [37] El Nahrawy, A., Salah. El-Deen, H., Soliman, A., Mosa, W., Crystallographic and Magnetic Properties of Al_3 -co-doped $\text{NiZnFe}_2\text{O}_4$ Nanoparticles Prepared by Sol-gel Process. *Egyptian Journal of chemistry*, Vol. 62, 2019, PP. 925-932.
- [38] El Nahrawy, A., Abou Hammad, A., Mansour, A., Preparation and Characterization of Transparent Semiconducting Silica Nanocomposites Doped with P_2O_5 and Al_2O_3 , *Silicon*, 2021.
- [39] Kumar, R., Selvam, N., Ragupathi, C., Kennedy, L., Vijaya, J., Synthesis, characterization and performance of porous Sr(II)-added ZnAl_2O_4 nanomaterials for optical and catalytic applications, *Powder Technology*, Vol. 224, 2012, PP. 147–154

- [40] El Nahrawy, A., Abou Hammad, A., Bakr, A., Shaheen, T., Mansour, A., Sol-gel synthesis and physical characterization of high impact polystyrene nanocomposites based on Fe₂O₃ doped with ZnO, *Applied Physics A*, Vol. 25, 2020.
- [41] Naskar, M., Chatterjee, M., A novel process for the synthesis of cordierite (Mg₂Al₄Si₅O₁₈) powders from rice husk ash and other sources of silica and their comparative study, *Journal of the European Ceramic Society*, Vol. 24, 2004, PP. 3499–3508.
- [42] Abou Hammad, A., Hemdan, B., El Nahrawy, A., Facile synthesis and potential application of Ni_{0.6}Zn_{0.4}Fe₂O₄ and Ni_{0.6}Zn_{0.2}Ce_{0.2}Fe₂O₄ magnetic nanocubes as a new strategy in sewage treatment, *Journal of Environmental Management* Vol. 270, 2020.
- [43] Shahi, A., Pandey, B., Singh, B., Gupta, B., Singh, S., Gopa, R., Photo Physical Studies of PVP Arrested ZnS Quantum Dots, *Electron. Mater. Lett.*, Vol. 13, 2017, PP. 160-167
- [44] Dahshan, A., Abou Hammad, A., Aly, K., El Nahrawy, A., Eu₂O₃ role in the optical and photoluminescence properties of 50 SiO₂ – 7 MgO – 20 ZnO_(23 - x) La₂O₃_x Eu₂O₃ nano-crystalline thin films, *Appl. Phys. A*, 126, 19 2020.
- [45] Vennila, R., Kamaraj, P., Arthanareeswarid, M., Sridharan, M., Sudha, G., Devikala, S., Arockiaselvi, J., Sivakumar, B., Banu, A., Rajeshwari, K., Biosynthesis of ZrO Nanoparticles And Its Natural Dye Sensitized Solar Cell Studies, *Materials Today: Proceedings* Vol.5, 2018, PP. 91–98
- [46] El-Nahrawy, A., Ali, A., Abou Hammad, A., Youssef, A., Influences of Ag-NPs doping chitosan/calcium silicate nano composites for optical and antibacterial activity, *International Journal of Biological Macromolecules*, Vol. 93, 2016, PP. 267–275.
- [47] Caglar, Y., Caglar, M., Ilıcan, S., Microstructural, optical and electrical studies on sol-gel derived ZnO and ZnO: Al films, *Current Applied Physics*, Vol. 12, 2012, PP. 963–968.
- [48] Xie, Y., Zhao, J., Le, Z., Li, M., Chen, J., Gao, Y., Huang, Y., Qin, Y., Zhong, R., Zhou, D., Ling, Y., Preparation and electromagnetic properties of chitosan-decorated ferrite-filled multi-walled carbon nanotubes/polythiophene composites, *Composites Science and Technology*, Vol. 99, 2014, PP. 141–146.
- [49] Abou Hammad, A., El Nahrawy, A., Atia, D., El-Madany, H., Mansour, A., Effect of Cu co-doping on the microstructure and optical properties of alumino-zinc thin films for optoelectronic applications, *Int. J. Materials Engineering Innovation*, Vol. 12, 2021.
- [50] Sharma, P., Sharma, V., Katyal, S., Variation of optical constant in Ge₁₀Se₆₀Te₃₀ thin film, *Chalcogen. Lett.*, Vol. 3, 2006, PP.73-79.